Structural, vibrational and luminescence properties of the (1–x)CaWO4–xCdWO4 system

A. Taoufyq, F. Guinneton, J-C. Valmalette, Madjid Arab, A. Benlhachemi, B. Bakiz, Sylvie Villain, A. Lyoussi, G. Nolibe, Jean-Raymond Gavarri

Structural, vibrational and luminescence properties of the $(1-x)\,CaWO_4-xCdWO_4$ system

A. Taoufyq [a,b,c,d], F. Guinneton [a], J-C. Valmalette [a], M. Arab [a], A. Benlhachemi [b], B. Bakiz [b], S. Villain [a], A. Lyoussi [c], G. Nolibe [d], J-R. Gavarri [a,*]

[a] Institut Matériaux Microélectronique et Nanosciences de Provence, Aix Marseille Université, CNRS, Université de Toulon, IM2NP UMR 7334, 83957, La Garde, France

[b] Laboratoire Matériaux et Environnement LME, Faculté des Sciences, Université Ibn Zohr, BP 8106, Cité Dakhla, Agadir, Maroc

[c] CEA/DEN, Département d'Études des Réacteurs, Laboratoire Dosimétrie Capteurs Instrumentation, CEA Cadarache, 13108, Saint-Paul-lez-Durance, France [d] Société CESIGMA, Signals & Systems, 1576 Chemin de La Planquette, 83130 La Garde, France

In the present work, we investigate the structural, microstructural, vibrational and luminescence properties of the system $(1-x)CaWO_4-xCdWO_4$ with x ranging between 0 and 1. Polycrystalline samples were elaborated using a coprecipitation technique followed by thermal treatment at 1000 °C. The samples were then characterized using X-ray diffraction, scanning electron microscopy, Raman spectroscopy and luminescence analyses. X-ray diffraction profile analyses using Rietveld method showed that two kinds of solid solutions $Ca_{1-x}Cd_xWO_4$ having scheelite and wolframite structures, with respectively tetragonal and monoclinic crystal cells, were observed, with a biphasic system for compositions $x=0.6$ and 0.7. The scanning electron microscopy experiments showed a complex evolution of morphologies and crystallite sizes as x increased. The vibration modes of Raman spectra were characteristic of composition-dependent disordered solid solutions with decreasing wavenumbers as x increased. Luminescence experiments were performed under UV-laser light irradiation. The energies of emission bands increased linearly with cadmium composition x. The integrated intensity of luminescence reached a maximum value for the substituted wolframite phase with composition $x=0.8$.

1. Introduction

The general aim of the present work is to correlate structural, vibrational and luminescence properties in the case of a solid solution based on calcium and cadmium tungstate phases. In the past, several systems based on calcium and cadmium tungstate ($CaWO_4$ and $CdWO_4$) were investigated for their potential applications in many fields such as photoluminescence [1–7], microwave applications [8–10], optical fiber scintillator material [11,12], humidity sensors and catalysis [13,14]. The two pure calcium and cadmium tungstate phases were previously synthesized by coprecipitation method [15,16], solid-state reaction [17–19], sol–gel method [16,20,21] and hydro/solvo-thermal method [22–25]. The $CaWO_4$ and $CdWO_4$ structures are strongly different, and belong respectively to the scheelite [12,19] (tetragonal) and wolframite [25,26] (monoclinic) systems. In the $CaWO_4$ and $CdWO_4$ structures, the tungsten atoms are bound respectively to four and six oxygen neighbors; the Ca and Cd ions form CaO_8 and CdO_6 polyhedra, respectively in the tetragonal and monoclinic structures. In other terms, [CaO_8–WO_4] and [CdO_6–WO_6] structural groups characterize the tetragonal and monoclinic phases, respectively.

In the present work, we investigate the structures and microstructures, the vibrational Raman spectra and the luminescence properties of this $(1-x)CaWO_4-xCdWO_4$ mix system. The phase diagram was partly determined in previous works [19]. As very few investigations on these solid solutions are available in the literature, we investigate a specific isotherm of the phase diagram by synthesizing various phases at 1000 °C. Finally, we attach particular importance to the study of the luminescence under UV excitation of this series of materials, with x varying between 0 and 1.

2. Experimental

2.1. Synthesis

Polycrystalline samples with nominal composition $Ca_{1-x}Cd_xWO_4$, with $0<x<1$ were prepared using the coprecipitation method

* Corresponding author. Tel: +33 494 142 311.
E-mail address: gavarri.jr@univ-tln.fr (J.-R. Gavarri).

[15,16]. The preliminary precursors were calcium and cadmium nitrate and sodium tungstate in aqueous solutions. The stoichiometric quantities of $Cd(NO_3)_2 \cdot 4H_2O$ [Sigma-Aldrich N° 20911, > 99.0%], $Ca(NO_3)_2 \cdot 4H_2O$ [Sigma-Aldrich N° C4955, > 99.0%] and $Na_2WO_4 \cdot 2H_2O$ [Sigma-Aldrich N° 72069, > 99.0%] were dissolved in 50 ml of distilled water individually for preparing 5 g of $Ca_{1-x}Cd_xWO_4$. The $Na_2WO_4 \cdot 2H_2O$ solution was added drop wise into the calcium and cadmium nitrate solutions under vigorous stirring. The precipitate was formed immediately at room temperature. Then, it was filtered out and washed with distilled water and finally ethanol. Finally, the solid precursors obtained by coprecipitation were heated under air at 1000 °C for 3 h.

2.2. Characterization techniques

2.2.1. X-ray diffraction

The polycrystalline samples were analyzed by X-ray diffraction (XRD), using the EMPYREAN Panalytical diffractometer, equipped with a copper X-ray source (wavelength $\lambda = 1.54 \times 10^{-10}$ m, tension $V = 45$ kV, intensity $I = 35$ mA), and with a Ni filter eliminating the $K\beta$ radiation. The diffractometer was equipped with a Pixcel-1D-Detector. The XRD analysis was carried out using the classical θ–2θ configuration, in continuous mode, with a step size of 0.0016413, a scan speed of 0.002°/s. All samples were powders compacted in a specific sample holder.

The various structural parameters of each sample were refined using Rietveld procedure. The FULLPROF program [27] was used to characterize the evolutions of the diffraction profiles and crystallographic parameters (cell parameters, coordinates of $M = Ca_{1-x}Cd_x$ and W atoms, Debye–Waller (DW) factors, full width at half maximum (FWHM)). In the refinement calculations, the oxygen coordinates previously determined by neutron diffraction by authors [28,29] were systematically fixed, because of the weak contribution of oxygen atoms to the structure factors and intensities in the case of X-ray diffraction. The atom coordinates and individual Debye factors B obtained by these authors [28,29] were used to initiate the refinements of the various structures.

2.2.2. Scanning electron microscopy analyses

Using a SUPRA 40 VP COLONNE GEMINI ZEISS scanning electron microscope (SEM), microstructural images were obtained with a maximum voltage of 20 kV. These analyses allowed analyzing the various morphologies of samples. X-ray emission from Energy Dispersive X-rays Spectroscopy (EDXS) allowed determining the grain compositions with a spatial resolution of 0.1 μm.

2.2.3. Raman spectroscopy analyses

Raman spectroscopy was used to characterize the evolution of the observed phases and to try to connect vibrational modes with these structural evolutions. The equipment used to perform the various vibrational spectra was a spectrometer Horiba Jobin-Yvon HR800 LabRam, spatially resolved to 0.5 μm, by means of an optical microscope with a 100× objective. The latter has a dual function: it allows first focusing the laser beam on a small area, and, second, visualizing the area of the sample. The 514.5 nm line of an Ar-ion laser was used as the excitation source; the photonic power applied to the samples was limited to 5 μW with an acquisition time of 30 s. Each Raman emission band was characterized by its wavenumber (in cm^{-1}).

2.2.4. Luminescence

The equipment used to perform the measurements of luminescence under UV was the previously described spectrometer Horiba Jobin-Yvon HR800 LabRam. The entrance slit, positioned behind the filter, is a diaphragm whose diameter can range from 50 to 500 μm. The irradiated zone was limited to 1 μm in diameter for all samples. The polycrystalline samples were in form of compacted pellets obtained under a fixed pressure of 5 kbar. The spherical mirror, characterized by an 800 mm focal length, allows reflecting the scattered radiation from the input to the dispersive grating to obtain spectra slot. The 364.5 nm line of an Ar-ion laser was used as the excitation source. The power applied to the samples was fixed to 0.005 mW with an acquisition time set to 100 ms.

3. Results

3.1. Structural studies

X-ray diffraction patterns showed a strong evolution in the phase system as cadmium atom fraction increases. Fig. 1a, a′ and b, b′ shows the X-ray diffraction patterns of the $MWO_4 = Ca_{1-x}Cd_xWO_4$ samples with x varying between 0 and 1. In the two composition ranges $0 \le x < 0.6$ and $0.7 < x \le 1$, two solid solutions are observed with two structural types: calcium rich tetragonal scheelite and cadmium rich monoclinic wolframite. In scheelite and wolframite phases, the tetragonal and monoclinic cells are constituted of four and two formula units MWO_4, respectively.

The refinement results were obtained using the space groups $I4_1/a$ (tetragonal phases) and $P2/c$ (monoclinic phases). The atom coordinates and DW factors of the pure phases $CaWO_4$ and $CdWO_4$ were used to initiate the calculations. In a first step, these coordinates were fixed. The calcium site where substitution occurred was defined as being a mean atom $M = Ca_{1-x}Cd_x$, with occupancy factors of $(1-x)$ for Ca and x for Cd. To refine the structures, we first refined the cell parameters, the profile parameters, the global DW factors (noted as B). Individual DW factors of heavy atoms (W and Cd) were used to try to characterize the disordered local distortions involved by the substitution of Ca by Cd atoms.

Tables 1a and 1b give the refined structural parameters associated with the two solid solutions, as a function of composition x: lattice parameters, cell volumes, DW factors and the different factors of agreement between the observed and calculated profiles. In these two tables, we have reported the refined atomic coordinates for the MWO_4 phases, except for the two-phase system due to the complexity of the diffraction patterns.

In Fig. 2a and b, we have reported the observed and calculated profiles of the $Ca_{0.5}Cd_{0.5}WO_4$ phase belonging to the scheelite structural type, and of the $Ca_{0.2}Cd_{0.8}WO_4$ phase belonging to the wolframite structural type. The difference curves show a good agreement between the observed and calculated patterns.

In Table 1c, we report the lattice parameters of a two-phase system separating the two solid solution domains. No residual oxide phase was detected by XRD. These results are in agreement with the phase diagram previously proposed for this system by authors [19]. We have assessed the amount of scheelite and wolframite phases in each sample using the X'pert Highscore software (not the Fullprof software). The result of the calculation shows that, for the composition $x = 0.6$, the proportions of scheelite and wolframite phases should be of about 56% and 46%, respectively. In the case of composition $x = 0.7$, the corresponding proportions should be of 45% and 55%, respectively.

Fig. 3a and b shows the variations as a function of composition x of the volumes (Fig. 3a and a′) of formula units $V/4$ and $V'/2$ (V and V' being the cell volumes of scheelite and wolframite structures respectively), and of isotropic Debye–Waller factors (Fig. 3b and b′) associated with the $M = Ca_{1-x}Cd_x$ site. No variation of the DW factor of tungsten atom was observed in our refinements. Two types of evolutions for volumes and B factors are observed. For scheelite phases ($x < 0.6$), a strong decrease of volumes and a strong increase

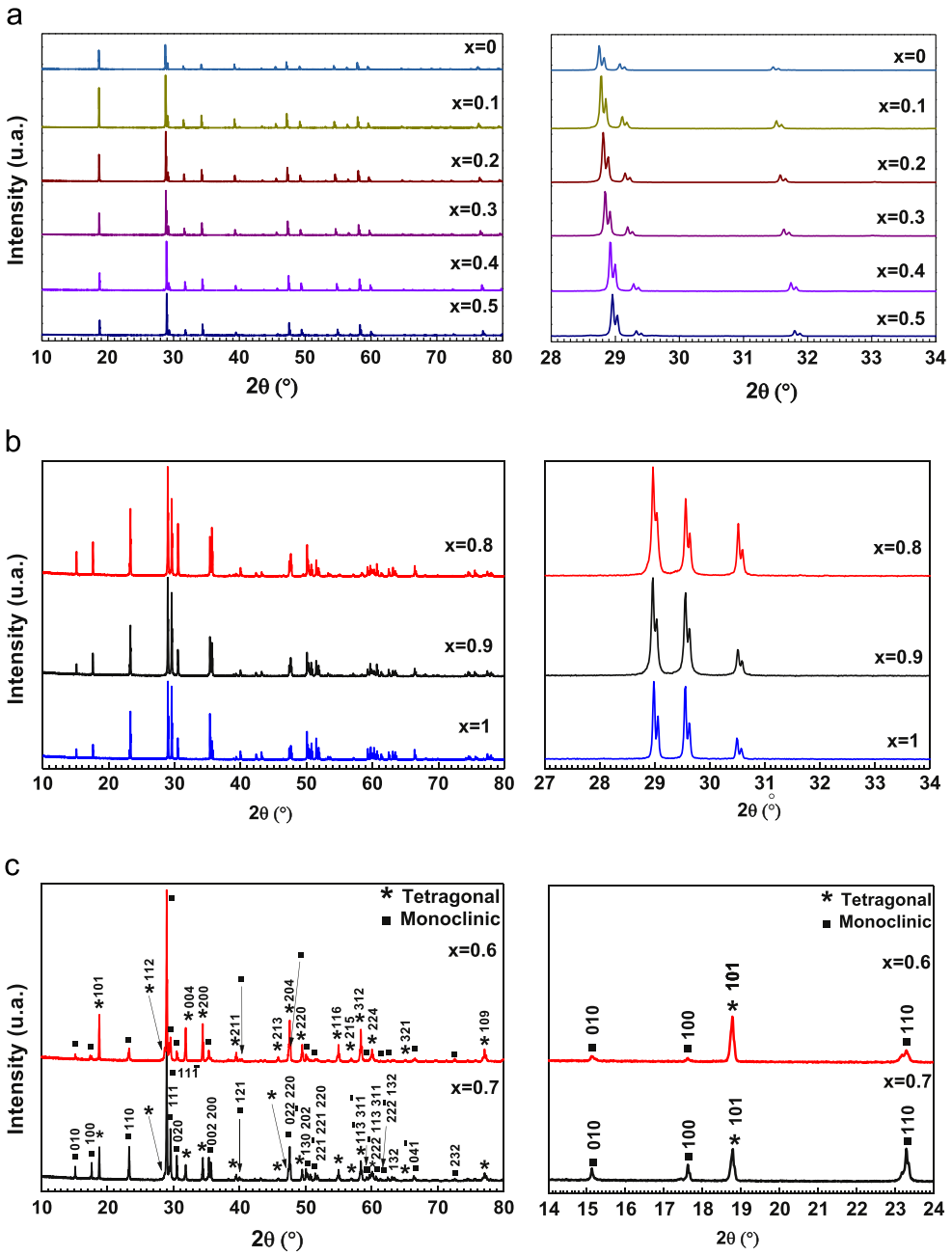

Fig. 1. (a) and (a′) XRD patterns of the $Ca_{1-x}Cd_xWO_4$ phase, $0 \le x \le 0.5$. (b) and (b′) XRD patterns of the $Ca_{1-x}Cd_xWO_4$ phase, $0.8 \le x \le 1$., (c) and (c′) XRD patterns of the $Ca_{1-x}Cd_xWO_4$ phase, $0.6 \le x \le 0.7$.

of B factors are observed as a function of x, in relation with the formation of disordered Cd–O–W links associated with distortions of $[MO_8–WO_4]$ groups with, probably, creation of $[CdO_6–WO_6]$ local defects. For wolframite phases ($x > 0.7$), a slight decrease in volume and a quasi-invariant B factor are observed: this would be due either to a partial substitution of Cd by Ca, or to unmodified volumes of the $[CaO_6–WO_6]$ groups. The quasi invariance of these volumes could be due to the ionic character of Ca–O bonds involving compensations in Ca–O–W links.

The fact that the DW factor of W atoms do not vary as a function of x argue in favor of the absence of defects in the W sites.

3.2. *Scanning electron microscopy*

The scanning electron analyses reported in Fig. 4 shows that the as-prepared powders generally consist of a complex distribution of different sizes of grains. A progressive evolution of morphologies is observed as x increases. In the range $0 < x < 1$ the morphologies and sizes can be described as follows:

- In the range of scheelite phases $0 < x < 0.5$ a bimodal distribution of grains is observed: as x increases, the initial regular shapes of $CaWO_4$ grains is changed into irregular and small grains;
- Samples $x = 0.6$ and 0.7 present new crystal shapes with a distribution of small grains;
- Samples $x = 0.8$ and 0.9 present large elongated crystals with well-defined facets and maximum linear dimensions (50 μm) for $x = 0.8$;
- Sample $x = 1$ present irregular crystal shapes with smooth surfaces, with crystallite sizes smaller than those observed in the sample $x = 0.8$.

Table 1a
Structural parameters for tetragonal solid solutions MWO_4 with $M=Ca_{1-x}Cd_x$. Space group: $I4_1/a$.

Composition x	0	0.1	0.2	0.3	0.4	0.5
a (10^{-10} m)	5.24254 (4)	5.23766(3)	5.23094(3)	5.22522(4)	5.21637(3)	5.20903(5)
$b=a$ (10^{-10} m)	5.24254(4)	5.23766(3)	5.23094(3)	5.22522(4)	5.21637(3)	5.20903(5)
c (10^{-10} m)	11.37479(9)	11.35339(9)	11.32743(3)	11.30540(9)	11.27345(8)	11.24792(9)
Volume cell (10^{-30} m^3): V	312.628(4)	311.459(4)	309.949(3)	308.671(4)	306.756(3)	305.201(5)
B (M)=($8\pi^2/3$).$\langle\Delta r^2\rangle$ (Å^2)	1.06(2)	1.20(3)	1.59(2)	1.77(4)	1.93(3)	2.15(2)
B (W) (Å^2)	0.75(1)	0.75(1)	0.75(1)	0.75(1)	0.75(1)	0.75(1)
Atom coordinates						
Ca (4a): (0, 0.25, z)	0.623(4)	0.628(3)	0.615(2)	0.632(3)	0.620(2)	0.638(3)
Cd (4a): (0, 0.25, z)	–	0.628(3)	0.615(2)	0.632(4)	0.620(2)	0.638(3)
W (4b): (0, 0.25, 0.125)	–	–	–	–	–	–
O (16f):(0.152, 0.005, 0.218)	(**)	(**)	(**)	(**)	(**)	(**)
Reliability factors (*)						
R_B %	6.81	7. 23	7.80	8.50	9.39	10.32
R_F (%)	5.14	5.57	5.34	7.51	5.65	8.49
R_{exp} (%)	6.38	6.04	6.43	6.58	6.80	6.77

Notes:
(*) $R_B=100\times\{\sum|I_k^{obs}-I_{ki}^{calc}|/\sum|I_k^{obs}|\}$; $R_F=100\times\{\sum|F_k^{obs}-F_{ki}^{calc}|/\sum|F_k^{obs}|\}$; $R_{exp}=100\times\{[(N-P+C)/\sum w_i|y_i^{obs}|^2]^{1/2}\}$.
Where N, P and C are the number of observations, parameters and constraints, respectively.
(**) Oxygen positions from authors [28] have been fixed; variable coordinates of Ca and W have been refined.

Table 1b
Structural parameters for monoclinic solid solutions MWO_4 with $M=Ca_{1-x}Cd_x$. Space group: $P2/c$.

Composition x	0.8	0.9	1
a (10^{-10} m)	5.03524(3)	5.03386(2)	5.03095(4)
b (10^{-10} m)	5.85657(2)	5.85542(2)	5.85455(3)
c (10^{-10} m)	5.07606(3)	5.07513(5)	5.07447(3)
β (°)=(a,c)	91.5663(4)	91.547(3)	91.527(5)
Volume cell (10^{-30} m^3): V	149.492(4)	149.474(3)	149.451(3)
B (M)=($8\pi^2/3$). $\langle\Delta r^2\rangle$ (Å^2)	0.86(2)	0.85(1)	0.82(2)
B (W) (Å^2)	0.48(1)	0.48(1)	0.48(1)
Atom coordinates			
Cd (2e): (0, y, 0.25)	0.190(2)	0.184(3)	0.196(3)
Ca (2e): (0, y, 0.25)	0.190(2)	0.184(3)	–
W (4f): (0.5, y, 0.25)	0.676(2)	0.678(3)	0.675(2)
O1 (4g): (0.297, 0.404, 0.048)	(**)	(**)	(**)
O2 (4g):(0.259, 0.129, 0.618)	(**)	(**)	(**)
Reliability factors			
R_B (%)	7.52	7.23	6.89
R_F (%)	6.24	6.13	5.78
R_{exp} (%)	7.87	6.76	6.16

Notes:
(*) $R_B=100\times\{\sum|I_k^{obs}-I_{ki}^{calc}|/\sum|I_k^{obs}|\}$; $R_F=100\times\{\sum|F_k^{obs}-F_{ki}^{calc}|/\sum|F_k^{obs}|\}$; $R_{exp}=100\times\{[(N-P+C)/\sum w_i|y_i^{obs}|^2]^{1/2}\}$.
Where N, P and C are the number of observations, parameters and constraints, respectively.
(**) Oxygen positions from authors [29] have been fixed; variable coordinates of Ca and W have been refined.

We summarize these observations in Table 2. In this table, we also report the X-ray emission analyses of the heavy atoms Ca, Cd, W. The EDX statistical chemical analysis is in relatively good agreement with nominal composition x. Specific EDX analyses of the largest individual crystallites (mainly for compositions $x=0.8$, 0.9 and 1, see Fig. 4) delivered compositions closely related to the mean composition x_{exp} determined in Table 2.

3.3. Raman spectroscopy analyses

Fig. 5a–c report the Raman spectra of scheelite and wolframite type solid solutions and of the biphasic system.

In the case of $CaWO_4$ and $CdWO_4$ structures, detailed attributions of vibration modes were previously proposed by authors Cavalcante et al. [31] and Chang Sung Lim [32]. Generally these modes were classified into two categories: the internal and the external modes. In their work on solid solution $Ca_{1-x}Sr_xWO_4$, the authors [33] also proposed a similar attribution of vibration modes.

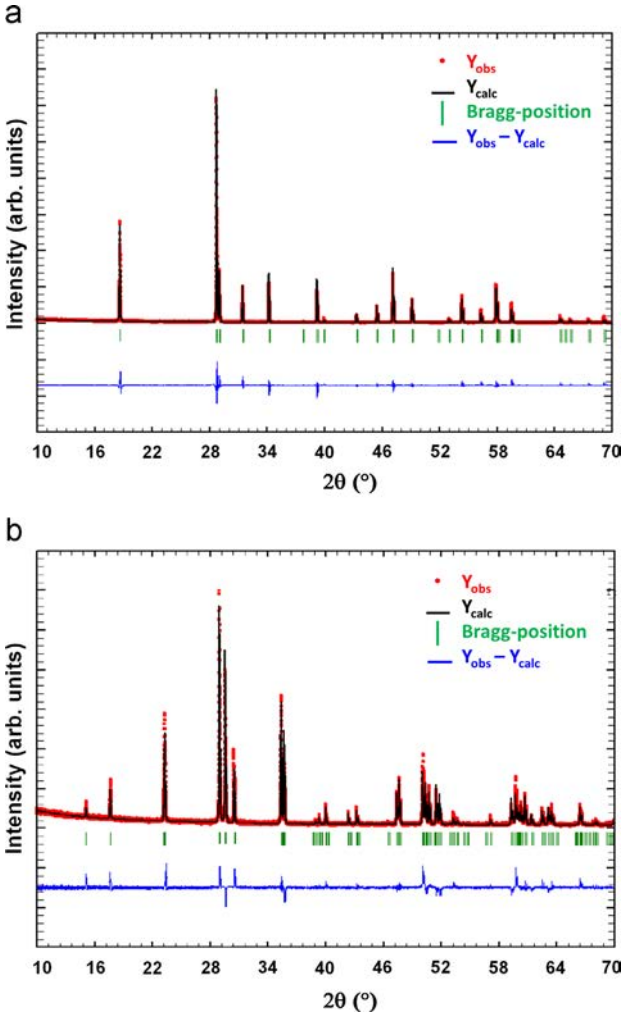

Fig. 2. (a) and (b) Calculated and observed diffraction profiles from Rietveld analysis for the samples of $Ca_{1-x}Cd_xWO_4$ phases. (a) $x=0.5$ (space group $I4_1/a$); (b) $x=0.8$ (space group $P2/c$).

Table 1c
Lattice parameter and cell volume of the two-phase system of $Ca_{1-x}Cd_xWO_4$ ($x=0.6$ and $x=0.7$) calculated by PARAM [30]software. Standard deviations in parentheses.

Tetragonal system	a (10^{-10} m)		c (10^{-10} m)		V (10^{-30} m^3)
$Ca_{0.4}Cd_{0.6}WO_4$	5.202(4)		11.223(4)		303.70(9)
$Ca_{0.3}Cd_{0.7}WO_4$	5.192(6)		11.215(2)		302.62(7)
Monoclinic system	a (10^{-10} m)	b (10^{-10} m)	c (10^{-10} m)	β (°)	V (10^{-30} m^3)
$Ca_{0.4}Cd_{0.6}WO_4$	5.042(9)	5.859(2)	5.079(9)	91.62(3)	149.64(8)
$Ca_{0.3}Cd_{0.7}WO_4$	5.037(2)	5.857(3)	5.075(2)	91.57(1)	149.57(9)

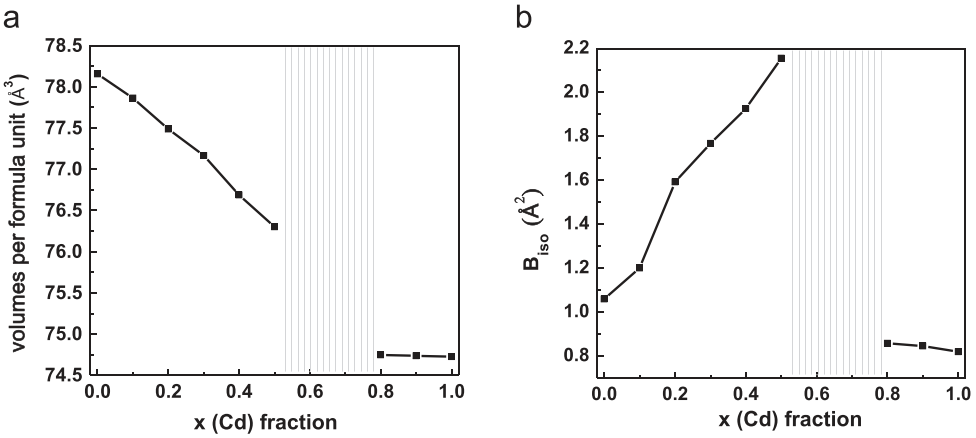

Fig. 3. ((a) and (a′)) Variations of the volumes per formula unit $V/4$ (scheelite) and $V'/2$ (wolframite); ((b) and (b′)) variation of the Debye–Waller factor B of $M=Ca_{1-x}Cd_x$ mean atom for scheelite structure (b) and for wolframite structure (b′), vs. composition x.

Scheelite structures. The group theory shows that the $CaWO_4$ crystals have 26 distinct vibration modes (Raman and infrared), as indicated in equation:

$$\Gamma_{(\text{Raman + Infrared})} = 3A_g + 5A_u + 5B_g + 3B_u + 5E_g + 5E_u$$

Thirteen of these vibration modes noted as $3A_g+5B_g+5E_g$ belong to the Raman active modes [31,34,35].

Finally, the Raman active vibration modes in $CaWO_4$ (wavenumbers ν in cm^{-1}, in parentheses) were decomposed as follows:

$$\Gamma_{(\text{Raman, internal})} = A_g(910) + B_g(838) + E_g(795) + B_g(399) + A_g(333) + B_g(333)$$

$$\Gamma_{(\text{Raman, external})} = E_g(274) + B_g(210) + E_g(194) + E_g(115) + B_g(80)$$

Wolframite structures. Thirty-six distinct vibration modes are expected in Raman (18 modes) and Infrared (18 modes) spectra as represented by Eq. below [36–38]:

$$\Gamma_{(\text{Raman + infrared})} = 8A_g + 10B_g + 8A_u + 10B_u$$

The internal and external Raman active modes can be represented by:

$$\Gamma_{(\text{Raman, internal})} = 4A_g + 2B_g \quad \text{and} \quad \Gamma_{(\text{Raman, external})} = 4A_g + 8B_g$$

Finally, the Raman active vibration modes in $CdWO_4$ (wavenumbers ν in cm^{-1}, in parentheses) were decomposed as follows:

$$\Gamma(\text{Raman, internal}) = A_g(895) + B_g(768) + B_g(685) + A_g(545) + A_g(385) + A_g(303)$$

$$\Gamma(\text{Raman, external}) = B_g(75) + A_g(97) + B_g(115) + B_g(132) + B_g(146) + A_g(175) + A_g(227) + B_g(247) + B_g(267) + B_g(350) + B_g(512) + A_g(706)$$

Fig. 6 represent the wavenumber variation with composition x of the A_g mode located at 910 cm^{-1} in the case of scheelite $CaWO_4$ structure, and of the A_g mode located at 895 cm^{-1} in the case of wolframite structure. These vibration modes, denoted A_g (910) and A_g (895), are generally attributed to the symmetrical vibrations of WO_4 and WO_6 groups.

In the scheelite solid solution ($x<0.6$) the small evolution of this wavenumber (910 cm^{-1}) as x increases is connected with the formation of Cd–O–W links in increasing proportion and local modifications of [CaO_8–WO_4] structural groups due to the substitution of Ca by Cd ions. In addition, the distribution of the structural groups [CdO_8–WO_4] is disordered: no superstructure is observed in our X-ray studies. For compositions $x>0.7$, in wolframite solid solution, the wavenumber of the corresponding mode (895 cm^{-1}) varies very slightly with respect to x: similarly, the volume of the formula unit MWO_4 varies little. In this monoclinic structure, this means that the volume of structural groups [MO_6–WO_6] and the A_g mode of WO_6 octahedra are not strongly perturbed by calcium substitution. This might be ascribed to the high ionic character of Ca–O bonds compared to the relative covalence of the Cd–O bonds: the total dimension of M–O–W links should be quasi invariant in the [MO_6–WO_6] groups.

In Tables 3a, 3a′, 3b and 3b′, we have reported the various attributions of the vibration modes observed as x increases. In the case of scheelite solid solution, the continuous decrease of the wavenumbers ν of Raman active modes confirms the substitution effect of Ca by Cd cations, with presence of disordered distribution of CdO_8 clusters in the solid solutions. It should be noted that, in scheelite structure, CdO_8–WO_4 groups constitute the major defects with progressive modifications of W–O lengths due to the covalent Cd–O bonds. Consequently, the hypothesis of existence of CdO_6–WO_6 configurations in these scheelite structures cannot be confirmed.

Considering these data, the observed vibration modes can be separated into two categories: a first category clearly depending on composition x and linked to significant W–O–Cd interactions, a second category, very weakly depending on composition x. In the

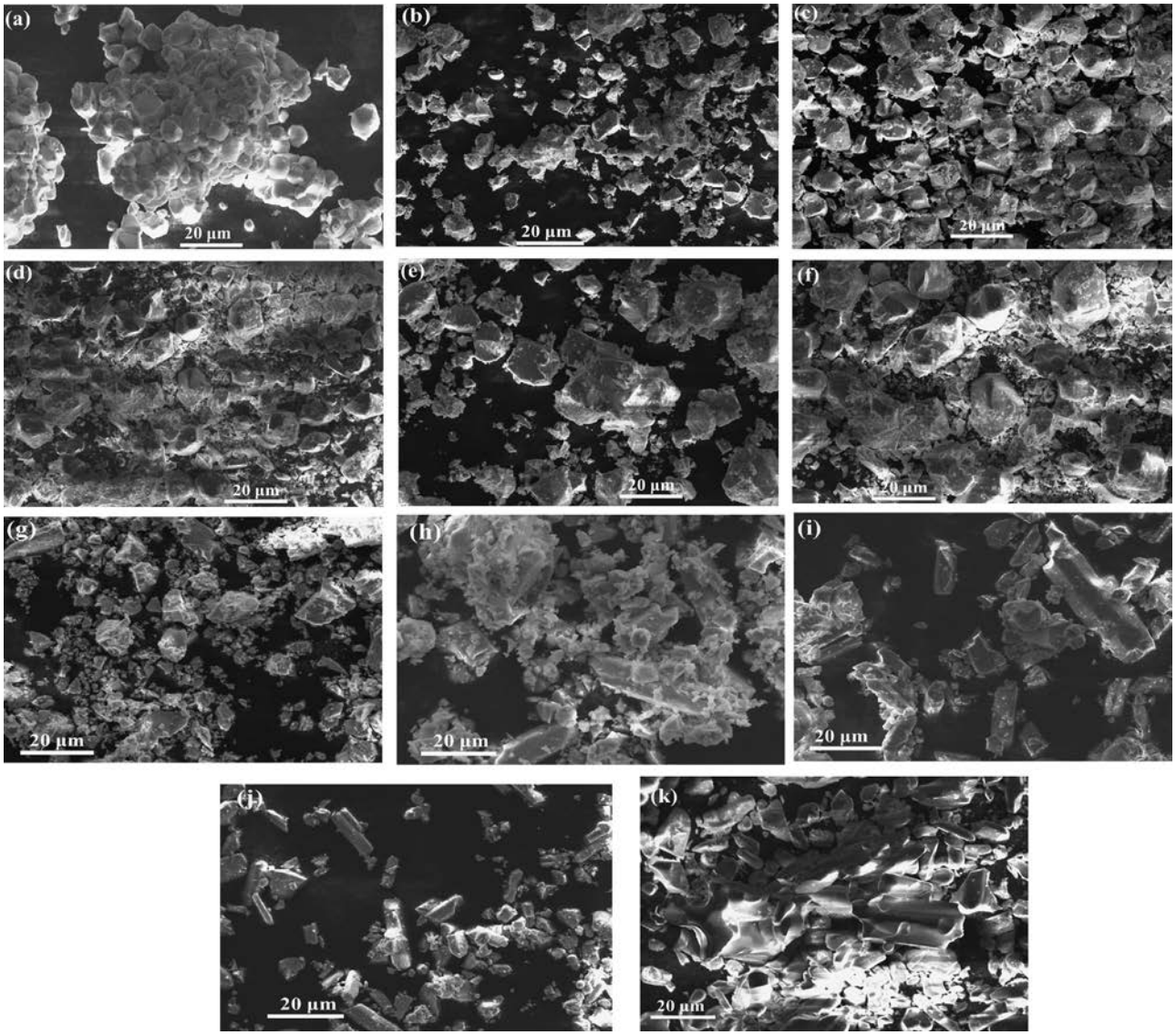

Fig. 4. Scanning electron microscopy analysis of the $Ca_{1-x}Cd_xWO_4$ phase (a) $x=0$, (b) $x=0.1$, (c) $x=0.2$, (d) $x=0.3$, (e) $x=0.4$, (f) $x=0.5$, (g) $x=0.6$, (h) $x=0.7$, (i) $x=0.8$, (j) $x=0.9$ and (k) $x=1$.

Table 2
SEM analyses. Evolution of grain sizes and morphologies. Atom fraction analyses of the heavy atoms Ca, Cd, W. Values x_{exp} from EDX analyses.

x	**0**	**0.1**	**0.2**	**0.3**	**0.4**	**0.5**
Size distribution	5–10 μm	5–10 μm	5–15 μm	5–15 μm	1–18 μm	1 to 20 μm
Shapes	Isotropic, square facets	Irregular, square facets	Irregular, square facets	Irregular, square facets	Irregular, square facets	Irregular, square facets
Ca (at%)	51.2	45.2	39.7	35.9	30.5	25.1
Cd (at%)	0.00	4.8	8.8	14.3	18.6	24.8
x_{exp}	0	0.10	0.18	0.28	0.38	0.50
W (at%)	48.8	50.0	51.5	49.8	50.9	50.2
x	**0.6**	**0.7**	**0.8**	**0.9**	**1**	
Size distribution	1 to 10 μm	1 to 40 μm	1 to 50 μm	1 to 15 μm	5 to 20 μm	
Shapes	Irregular	Long crystals	Long and large crystals	Long and small bars	Irregular	
Ca (at%)	20.1	15.2	9.88	4.6	0.00	
Cd (at%)	29.2	34.2	40.7	44.6	50.9	
x_{exp}	0.59	0.69	0.80	0.91	1	
W (at%)	50.7	51.6	49.42	50.8	49.1	

tables, we have indicated the two rates of change $\Delta\nu/\nu$. In the case of wolframite solid solutions ($0.8 < x < 1$), we observe a quasi-invariance of vibrational bands as calcium composition $y=1-x$ increases.

4. Luminescence properties

The UV-laser light luminescence spectra obtained under UV excitation ($\lambda_{exc}=364.5$ nm), are presented in Fig. 7a–d. Each

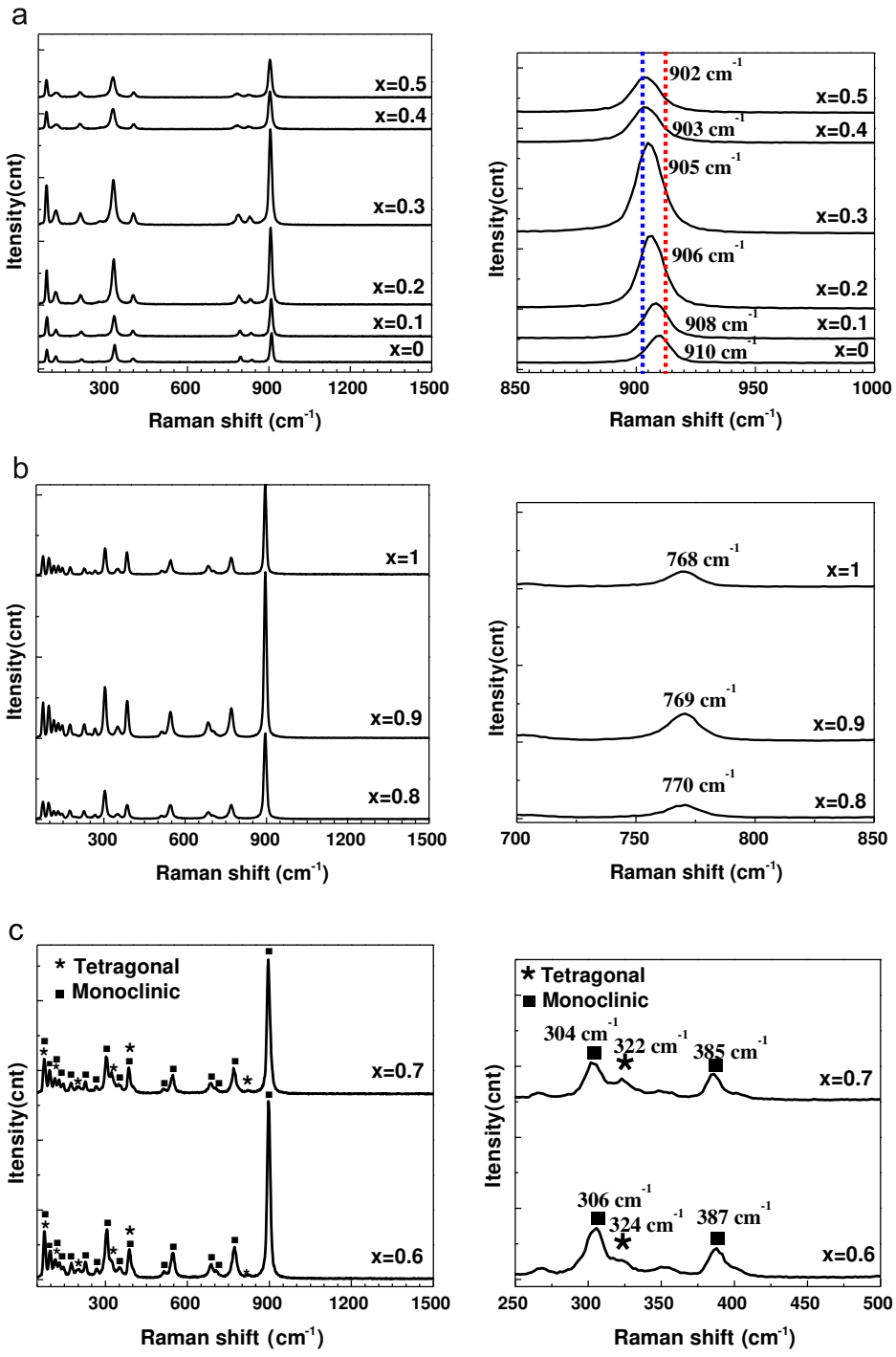

Fig. 5. (a) and (a′) Raman spectra (λ=514.5 nm) of the $Ca_{1-x}Cd_xWO_4$ phase, $0 \le x \le 0.5$. (b) and (b′) Raman spectra (λ=514.5 nm) of the $Ca_{1-x}Cd_xWO_4$ phase, $0.8 \le x \le 1$ c), (c′) Raman spectra (λ=514.5 nm) of the two-phase system, $0.6 \le x \le 0.7$.

emission band will be characterized by:

- The intensity $I(\lambda, x)$ for a fixed wavelength and fixed composition x;
- The wavelength of its maximum intensity $I(\lambda, x)$, noted $\lambda_{max}(x)$ and corresponding to an energy E_{max};
- Its integrated intensity $I(x)=\int I(\lambda, x)\, d\lambda$ (surface of emission band).

The profiles of the luminescence spectra of $CaWO_4$ and $CdWO_4$ were previously interpreted [31–33]. All our spectra present similar profiles, in agreement with these previous works. In Table 4, we have reported the integrated intensities $I(x)$ and the wavelengths $\lambda_{max}(x)$.

In Fig. 8a and b, we have represented the evolution with composition x of the energy E_{max} (x)=associated with λ_{max} and of the luminescence intensity $I(x)$. We observe increasing values of E_{max} and irregular values of $I(x)$: the main feature resides in the strong amplification observed close to the x=0.8 composition value. The intensity $I(x=0.8)$ is more than hundred times higher than that observed for $CaWO_4$ and roughly 30 times higher than that observed for $CdWO_4$.

Orhan et al. [39] and Pôrto et al. [33] attributed their luminescence analyses to specific allowed electronic transitions between W* antibonding levels and oxygen O2*p* bonding levels, characteristic of tungstate groups. The authors [33,39] also interpreted the

strong variations of emission intensities from the existence of several types of defects resulting from elaboration conditions:

- presence of WO_3 clusters among the WO_4 expected clusters,
- presence of vacancies in WO_4 clusters described as $[WO_3\square]$ charged clusters;

Tingjiang et al. [26] showed in their band structure calculation for the monoclinic $CdWO_4$ that the conduction band was dominated by O 2*p*, W 5*d*, and Cd 5*s* orbitals, while the valence band was mainly composed of the O 2*p* and W 5*d* orbitals.

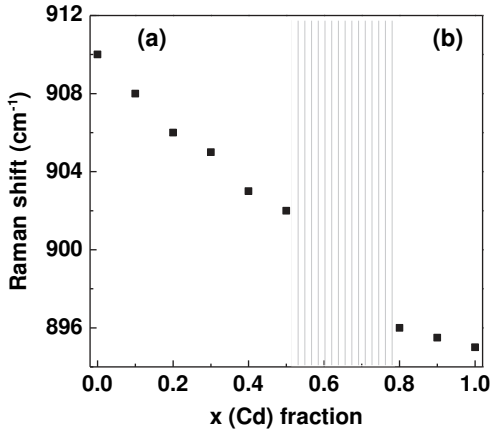

Fig. 6. Variation as a function of x of the A_g mode (a) scheelite structure (b) wolframite structure vs comparition X.

In our experiments, the energy E_{max}, increasing with composition x, can be associated with the progressive modification of the O 2*p* and W 5*d* orbitals by hybridization with Cd orbitals. The evolution of intensities of luminescence bands is characterized by a strong increase with a maximum value for the intermediate composition $x=0.8$. It should be noted that maximum crystal sizes have been observed for this composition $x=0.8$.

To try to connect crystallization effect and luminescence intensity, we have performed a new series of luminescence analyses on samples of composition $x=0.8$, prepared in different conditions, including samples subjected to different types of grindings. We have reported the results in Table 4. A similar amplification of luminescence has been systematically observed with values having similar order of magnitudes (intensity variation of about 2 to 3%). So, the unique origin of this observed luminescence amplification cannot be ascribed to the sole size effect. In relation with the observations of authors [33] on their $Ca_{1-x}Sr_xWO_4$ solid solution, this observation can be related first to the role of calcium on crystallization during elaboration process. For composition $x=0.8$, two effects must be taken into account:

- Optimization of crystal growth of wolframite phase due to presence of calcium, with well-ordered lattice associated with well-defined surfaces of crystals (see Fig. 3);

Table 3a
Raman spectroscopy data of tetragonal solid solution $Ca_{1-x}Cd_xWO_4$ with $0 \le x \le 0.5$: wavenumbers of the internal vibration modes.

	A_g+B_g (333) WO_4 bending	B_g (399) WO_4 bending	E_g (795) WO_4 as-stretching	B_g (838) WO_4 as-stretching	A_g (910) WO_4 stretching
$x=0$	333	399	795	838	910
$x=0.10$	330	398.9	793	835	908
$x=0.20$	328	398.8	790	831	906
$x=0.30$	327	398.7	786	828	905
$x=0.40$	325	398.5	783	825	903
$x=0.50$	324	398.4	781	824	902
$\Delta\nu/\nu$	0.027	0.001	0.018	0.017	0.009

Note: as-stretching=antisymmetric stretching; ν=Raman shift in cm^{-1}; $\Delta\nu/\nu=[\nu(x=0)-\nu(x=0.5)]/\nu(x=0)$.

Table 3a′
Raman spectroscopy data of tetragonal solid solution $Ca_{1-x}Cd_xWO_4$ **with $0 \le x \le 0.5$: wavenumbers of the external vibration modes.**

	B_g (80) CaO_8 bending	E_g (115) CaO_8 bending	E_g (194) (*) CaO_8 stretching	B_g (210) CaO_8 stretching	E_g (274) WO_4 torsion
$x=0$	81.0	115.9	194	210	274
$x=0.10$	80.6	115.7	(*)	208	273
$x=0.20$	80.5	115.6	(*)	207	272
$x=0.30$	80.5	115.4	(*)	205	272
$x=0.40$	80.4	115.4	(*)	203	272
$x=0.50$	80.3	115.3	(*)	202	272
$\Delta\nu/\nu$	0.008	0.005	(*)	0.038	0.007

Note: ν=Raman shift in cm^{-1} ; $\Delta\nu/\nu=[\nu(x=0)-\nu(x=0.5)]/\nu(x=0)$; (*) this mode vanished for $x>0$.

Table 3b
Raman spectroscopy data of monoclinic solid solution $Ca_{1-x}Cd_xWO_4$ with $0.8 \le x \le 1$: wavenumbers of the internal vibration modes.

	A_g (303) CdO_6 stretching	A_g (385) WO_6 stretching	A_g (545) W–O–W stretching	B_g (685) WO_6 as-stretching	B_g (768) WO_6 as-stretching	A_g (895) WO_6 stretching
$x=1$	303	385	545	685	768	895
$x=0.9$	303.4	385.5	545.4	685.5	769	895.5
$x=0.8$	303.8	386	546	686	770	896
$\Delta\nu/\nu$	0.0026	0.0026	0.0018	0.0014	0.0025	0.0011

Table 3b′
Raman spectroscopy data of monoclinic solid solution $Ca_{1-x}Cd_xWO_4$ **with $0.8 \le x \le 1$: wavenumbers of the external vibration modes.**

	B_g (75) CdO_8 bending	A_g (97) CdO_8 bending	B_g (115) CdO_8 stretching	B_g (132) CdO_8 stretching	E_g (146) WO_6 torsion	A_g (175) CdO_8 bending
$x=1$	75	97	115	132	146	175
$x=0.9$	75.3	97.2	115.5	132.4	146.5	175.3
$x=0.8$	75.5	97.6	115.8	133	147	175.8
$\Delta\nu/\nu$	0.006	0.006	0.0069	0.0075	0.0068	0.0045
	A_g (227)) CdO_8 bending	B_g (247) CdO_8 stretching	B_g (267) CdO_8 stretching	E_g (349) WO_6 torsion	B_g (512) CdO_8 bending	A_g (706) CdO_8 bending
$x=1$	227	247	267	349	512	705.4
$x=0.9$	227.5	247.4	267.5	349.4	512.4	705.8
$x=0.8$	227.8	248	268	350	512.8	706
$\Delta\nu/\nu$	0.0035	0.0040	0.0037	0.0028	0.0015	0.0008

Note: ν=Raman shift in cm^{-1} ; $\Delta\nu/\nu = |[\nu(x=1)-\nu(x=0.8)]|/\nu(x=1)$.

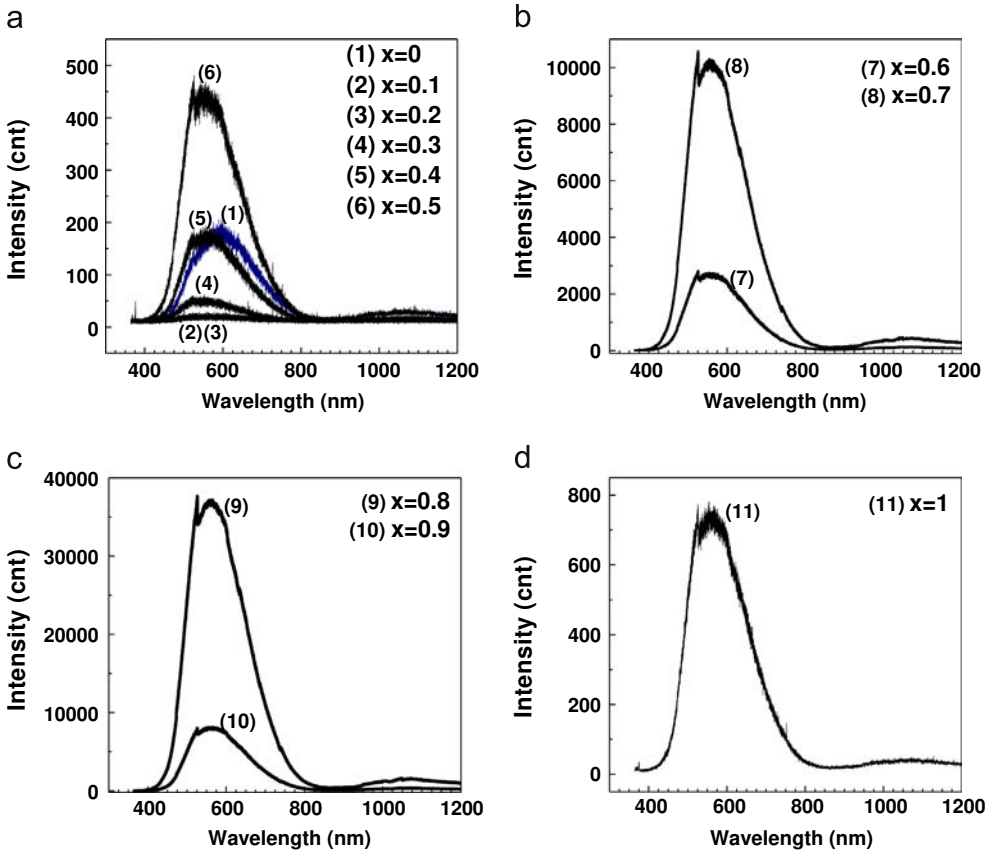

Fig. 7. Luminescence analyses on UV excitation (364.5 nm): Experimental emission bands of the $Ca_{1-x}Cd_xWO_4$ polycrystalline phases with; (a) $0 \le x \le 0.5$; (b) $0.6 \le x \le 0.7$; (c) $0.8 \le x \le 0.9$ and (d) Experimental emission band of $CdWO_4$. The intensity jump observed at a wavelength of 525 nm is due to spectrometer grating change.

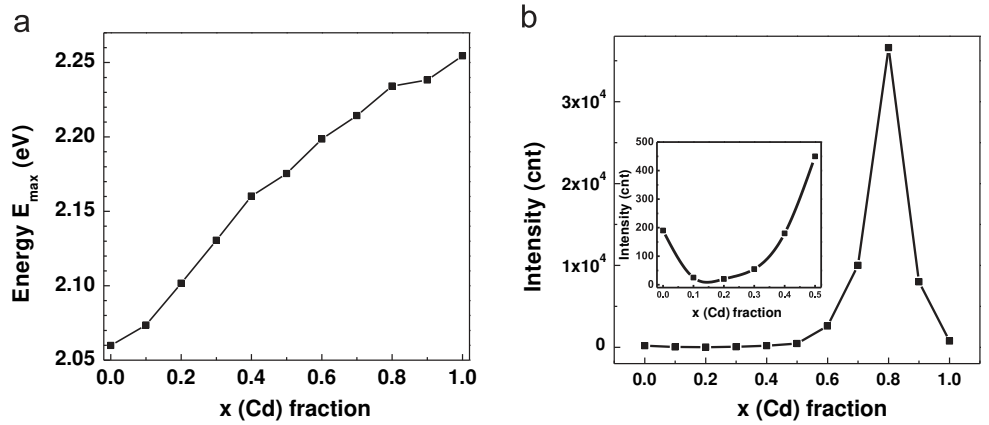

Fig. 8. (a) and (b) (a) Variation of the energy E_{max} corresponding to the maximum intensity of luminescence I_{max} and (b) integrated intensities I, as a function of x.

Table 4
Variation of the wavelength λ_{max} and integrated intensities $I(x)$ as a function of x. Effect of elaboration conditions.

	$x=0$	$x=0.1$	$x=0.2$	$x=0.3$	$x=0.4$	$x=0.5$	$x=0.6$	$x=0.7$	$x=0.8$	$x=0.9$	$x=1$
λ_{max} **(nm)**	602	598	590	582	574	570	564	560	555	554	550
I **(counts)**	190	25	20	55	180	450	2600	10,000	36,600	8000	755
Samples with composition $x=0.8$											
Samples	SS-1000 °C		Cop-1000 °C		Cop-1100 °C		Cop-1200 °C		Cop-1000 °C-Gr1		Cop-1000 °C-Gr2
	Solid state reaction + thermal treatment at 1000 °C/10 h		Coprecipitation + thermal treatment at 1000 °C/3 h		Coprecipitation + thermal treatment at 1100 °C/3 h		Coprecipitation + thermal treatment at 1200 °C/3 h		Coprecipitation + thermal treatment at 1000 °C/3 h + grinding process (15 min)		Coprecipitation + thermal treatment at 1000 °C/3 h + grinding process (30 min)
Integrated intensity $I(x=0.8)$, with invariant wavelength $\lambda_{max}=555$ nm											
$I(x=0.8)$	34,800		36,600		35,300		35,000		36,000		35,700

- Presence of structural defects linked to $[CaO_6–WO_6]$ disordered groups (e.g. 20 mol%) substituting for $[CdO_6–WO_6]$ groups, giving rise to large number of active sites for luminescence.

Finally, the luminescence of our as prepared wolframite phase $Ca_{0.20}Cd_{0.80}WO_4$ should be conditioned by the juxtaposition of an ordered host lattice and a distribution of disordered $[CaO_6–WO_6]$ groups having luminescence activity based on specific charge transfer $W^*(5d)\rightarrow O(2p)$.

This should be in full agreement with the interpretation given by authors [33] to justify the maximum of luminescence in their specific sample $Ca_{0.4}Sr_{0.6}WO_4$: the optimized luminescence should be reached in samples neither excessively ordered nor excessively disordered. Let us recall at this point that the authors [39] have already shown that the maximum luminescence intensity was reached for samples having intermediate defect amounts due to diversified thermal treatments. They considered that luminescence should be maximum for samples being neither excessively ordered nor excessively disordered. It should be added that such increased luminescence (as in our samples with $0.6<x<0.9$) could be due to the formation of well-defined surfaces of large crystals, with good optical properties, including a regular distribution of active defects allowing intense photonic emission.

Correlatively, the intensity decrease observed in our experiments in the composition range $0<x<0.3$ might be the result of irregular morphologies with a large number of surface defects and high disorder of $[CdO_8–WO_4]$ groups in the scheelite lattice.

5. Conclusions

In this study, we have synthesized two types of solid solutions $Ca_{1-x}Cd_xWO_4$ having scheelite and wolframite structures and a two-phase system from a coprecipitation method followed by thermal treatment at 1000 °C. Samples with compositions $x=0.6$ and 0.7 belong to the two-phase system. In the XRD analyses of calcium rich scheelite phases, we have shown that a Debye–Waller factor, associated with the substitution of Ca by Cd in the scheelite structure, can be used to characterize the structural modifications or distortions due to Cd substitution. In the WO_4 tetrahedra or WO_6 octahedra, no significant disorder is observed. In the case of cadmium rich solid solution, structural distortions are very weak.

In the Raman spectroscopy analyses, the two solid solutions are characterized by two kinds of modes belonging to the two structural symmetries. The decrease of wavenumber observed as x increases is directly associated with modifications of WO_4 or WO_6 vibration modes, due to the mass effect involved by Cd–O bonds through Cd–O–W links, and also due to modifications in W–O and M–O distances. It should be noted that the linear evolutions of Raman shifts fully confirms the disordered nature of the solid solutions in this composition range.

The energy of the emission bands increases linearly with x. The increasing energies of emission bands is interpreted in terms of progressive modification of charge transfer linked to the transition $W^*(5d)\rightarrow O(2p)$: this modification might be ascribed to the contribution of Cd hybridized orbitals in the bottom of conduction bands. The most striking result is the high luminescence intensity observed for the composition $x=0.8$. The analyses of luminescence show a strong increase of the intensities above $x=0.3$ with a maximum for the composition $x=0.8$. This maximum should be directly due to the perturbation of $[CdO_6–WO_6]$ groups by Ca^{2+} ions, associated with specific crystal shapes observed in the composition range 0.6 to 0.9. These results tend to confirm the above interpretations given by authors [33,39].

Acknowledgments

This work was financially supported by the Regional Council of Provence-Alpes—Côte d'Azur, the European Funds for Regional Development, the General Council of Var and by Toulon Provence Mediterranean, in the general framework of NANOGAMMA project (Grant number: 2010-16028/42169; collaboration between IM2NP, CEA of Cadarache, CESIGMA and IBS Societies) and international ARCUS-CERES project.

References

[1] L. Gracia, Valéria M. Longo, Laécio S. Cavalcante, A. Beltrán, W. Avansi, M.S. Li, V.R. Mastelaro, J.A. Varela, E. Longo, J. Andrés, J. Appl. Phys. 110 (4) (2011) 043501.
[2] H.F. Hameka, C.C. Vlam, Physica 19 (1953) 943–949.
[3] T. Thongtem, S. Kungwankunakorn, B. Kuntalue, A. Phuruangrat, S. Thongtem, J. Alloys Compd. 506 (2010) 475–481.
[4] D. Spassky, V. Mikhailin, M. Nazarov, M.N. Ahmad-Fauzi, A. Zhbanov, J. Lumin. 132 (2012) 2753–2762.
[5] V.B. Mikhailik, H. Kraus, D. Wahl, M. Itoh, M. Koike, I.K. Bailiff, J. Phys. Rev. B 69 (20) (2004) 205110–205110-9.
[6] R. Grasser, A. Scharmann, J. Lumin 12-13 (1976) 473–478.
[7] W. Zhang, J. Long, A. Fan, J. Li, J. Mater. Res. Bull. 47 (2012) 3479–3483.
[8] J.C. Sczancoski, L.S. Cavalcante, M.R. Joya, J.A. Varela, P.S. Pizani, E. Longo, J. Chem. Eng 140 (2008) 632–637.
[9] T. Thongtem, A. Phuruangrat, S. Thongtem, J. Mater. Lett. 62 (2008) 454–457.
[10] J. Liu, J. Ma, B. Lin, Y. Ren, X. Jiang, J. Tao, X. Zhu, Ceram. Int. 34 (2008) 1557–1560.
[11] M. Nikl, P. Bohacek, E. Mihokova, N. Solovieva, A. Vedda, M. Martini, G.P. Pazzi, P. Fabeni, M. Kobayashi, M. Kobayashi, J. Appl. Phys. 91 (8) (2002) 5041–5044.
[12] M Nikl, P Bohacek, E Mihokova, M Kobayashi, M Ishii, Y Usuki, V Babin, A Stolovich, S Zazubovich, M Bacci, J. Lumin. 87-89 (2000) 1136–1139.
[13] T. Thongtem, A. Phuruangrat, S. Thongtem, J. Ceram. Process. Res., 258–261 (2008).
[14] C.S. Lim, K.H. Kim, K.B. Shim, J. Ceram. Process. Res. 12 (6) (2011) 727–731.
[15] T. Thongtem, S. Kungwankunakorn, B. Kuntalue, A. Phuruangrat, S. Thongtem, J. Alloys Compd. 506 (1) (2010) 475–481.
[16] A. ManoPriya, R. KalaiSelvan, B. Senthilkumar, M.K. Satheeshkumar, C. Sanjeeviraja, J. Ceram. Int. 37 (7) (2011) 2485–2488.
[17] D.S Robertson, I.M Young, J. R Telfer, J. Mater. Sci. 14 (1979) 2967–2974.
[18] Luke L.Y. Chang, G. Margaret Scroger, B. Phillips, J. Am. Ceram. Soc. 49 (7) (1966) 385–390.
[19] L.Y. Chang Luke, Am. Mineral. 52 (1967) 427–435.
[20] A. Katelnikovas, L. Grigorjeva, D. Millers, V. Pankratov, A. Kareiv, Lith. J. Phys. 47 (1) (2007) 63–68.
[21] K. Lennstrom, S.J. Limmer, G. Cao, J. Thin Solid Films 434 (2003) 55.
[22] Y. Wang, J. Ma, J. Tao, X. Zhu, J. Zhou, Z. Zhao, L. Xie, H. Tian, J. Ceram. Int. 33 (2007) 11–25.
[23] Y. Ling, L. Zhou, L. Tan, Y Wang, C. Yu, J. Cryst. Eng. Comm 12 (2010) 3019–3026.
[24] W.S. Wang, L. Zhen, C.Y Xu, Li Yang, W.Z. Shao, J. Phys. Chem. C 112 (2008) 19390–19398.
[25] A.J. Rondinone, M. Pawel, D. Travaglini, S. Mahurin, S. Dai, J. Colloid Interface Sci. 306 (2) (2007) 281–285.
[26] Tingjiang Yan, Liping Li, Wenming Tong, Jing Zheng, Yunjian Wang, Guang she Li, J. Solid State Chem. 184 (2011) 357–364.
[27] T. Roisnel, J. Rodríguez-Carvajal, R. Delhez, E.J. Mittenmeijer (Eds.), in: Proceedings of the Seventh European Powder Diffraction Conference, Barcelona–Spain, 2000, pp. 118–123.
[28] R.M. Hazen, L.W. Finger, J.W.E. Mariathasan, J. Phys. Chem. Solids 46 (1985) 253–263.
[29] J. Macavei, H. Schulz, Z. Kristallogr. 207 (1993) 193–208.
[30] J.F Berar, Ecole Centrale de Paris, 92295 Châtenay—Malabry Private Communication, 1989.
[31] L.S. Cavalcante, V.M. Longo, J.C. Sczancoski, M.A. P. Almeida, A.A. Batista, J.A. Varela, M.O. Orlandi, E. Longoa, M. Siu Li, J. Cryst. Eng. Comm 14 (2012) 853–868.
[32] Chang Sung Lim, J. Mater. Chem. Phys. 131 (2012) 714–718.
[33] S.L. Pôrto, E. Longo, P.S. Pizani, T.M. Boschi, L.G.P. Simões, S.J.G. Lima, J.M. Ferreira, L.E.B. Soledade, J.W.M. Espinoza, M.R. Cassia-Santos, M.A.M. A. Maurera, C.A. Paskocimas, I.M.G. Santos, A.G. Souza, J. Solid State Chem. 181 (2008) 1876–1881.
[34] S. Yiguo, L Guangshe, X. Yanfeng, L. Liping, J. Phys. Chem. C 111 (2007) 6684–6689.
[35] A. Priya, E. Sinha, S.K. Rout, J. Solid State Sci. 20 (2013) 40–45.
[36] M. Saito, J. Suda, T. Sato, J. Spectrom. Soc. Jpn. 51 (2) (2002) 65–71.
[37] R.C. Dai, X. Ding, Z.P. Wang, Z.M. Zhang, J. Chem. Phys. Lett. 586 (2013) 76–80.
[38] L.S. Cavalcante, E. Moraes, M.A.P. Almeida, C.J. Dalmaschio, N.C. Batista, J.A. Varela, E. Longo, M. Siu Lid, J. Andrés, A. Beltrán, J. Polyhedron 54 (2013) 13–25.
[39] E. Orhan, M. Anicete-Santos, M.A. Maurera, M.F. Pontes, A.G. Souza, J. Andres, A. Beltran, J.A. Varela, P.S. Pizani, C.A. Taft, E. Longo, J. Solid State Chem. 178 (2005) 1284–1291.